

PARP-1-targeted Auger emitters display high-LET cytotoxic properties in vitro but show limited therapeutic utility in solid tumor models of human neuroblastoma

Authors

Hwan Lee¹, Aladdin Riad¹, Paul Martorano¹, Adam Mansfield¹, Minu Samanta², Vandana Batra², Robert H. Mach¹, John M. Maris², Daniel A. Pryma¹, and Mehran Makvandi¹

Affiliations

1. Department of Radiology, University of Pennsylvania Perelman School of Medicine, 3400 Spruce Street, Philadelphia, PA, 19104, USA

2. Division of Oncology and Center for Childhood Cancer Research, Children's Hospital of Philadelphia, 3401 Civic Center Boulevard, Philadelphia, PA, 19104, USA

Corresponding author

Name: Mehran Makvandi

Address: Donner D001031, HUP, 3400 Spruce Street, Philadelphia, PA, 19104

Telephone: 215-746-8755

Fax: 215-349-5843

Email: Makvandi@pennmedicine.upenn.edu

First author

Name: Hwan Lee

Address: 3400 Spruce Street, Philadelphia, PA, 19104

Telephone: 484-515-0922

Fax: 215-349-5843

Email: Hwan.Lee@pennmedicine.upenn.edu

In training: Resident

Disclosure

Funding support for the work was received through the United States Department of Energy grant DE-SC0017646 (R. Mach) and National Institutes of Health through the Research Project Grant R01-CA219006 (D. Pryma).

R.H.M., D.A.P., and M.M. are designated as inventors on a patent held by the University of Pennsylvania that describes the intellectual property associated with ²¹¹At-MM4 (WO2018218025A1). D.A.P. would like to disclose unrelated conflicts including honoraria and research support from Siemens, Progenics, and 511 Pharma, as well as honoraria from Actinium and Nordic Nanovector. All other authors declare no conflicts of interest.

Word count: 4,978

Running title: PARP-1-targeted Auger therapy

ABSTRACT

The currently available therapeutic radiopharmaceutical for high-risk neuroblastoma, ^{131}I -MIBG, is ineffective at targeting micrometastases due to the low linear energy transfer (LET) properties of high-energy beta particles. In contrast, Auger radiation has high-LET properties with nanometer ranges in tissue, efficiently causing DNA damage when emitted in close proximity to DNA. The aim of this study was to evaluate the cytotoxicity of targeted Auger therapy in pre-clinical models of high-risk neuroblastoma.

Methods: Using a radiolabeled poly(ADP-ribose) polymerase (PARP) inhibitor, ^{125}I -KX1, we delivered an Auger emitter iodine-125 to PARP-1: a chromatin-binding enzyme overexpressed in neuroblastoma. *In vitro* cytotoxicity of ^{125}I -KX1 was assessed in nineteen neuroblastoma cell lines, followed by in-depth pharmacological analysis in a sensitive and resistant pair of cell lines. Immunofluorescence microscopy was used to characterize ^{125}I -KX1-induced DNA damage. Finally, *in vitro/in vivo* microdosimetry was modeled from experimentally derived pharmacological variables. **Results:** ^{125}I -KX1 was highly cytotoxic *in vitro* across a panel of neuroblastoma cell lines, directly causing double strand DNA breaks. Based on subcellular dosimetry, ^{125}I -KX1 was approximately twice as effective compared to ^{131}I -KX1, whereas cytoplasmic ^{125}I -MIBG demonstrated low biological effectiveness. Despite the ability to deliver focused radiation dose to the cell nuclei, ^{125}I -KX1 remained less effective than its alpha-emitting analog ^{211}At -MM4, and required significantly higher activity for equivalent *in vivo* efficacy based on tumor microdosimetry. **Conclusion:** Chromatin-targeted Auger therapy is lethal to high-risk neuroblastoma cells with potential use in micrometastatic disease. This study provides the first evidence for cellular lethality from a PARP-1 targeted Auger emitter, calling for further investigation into targeted Auger therapy.

Key words: radiopharmaceutical therapy, Auger emitter, PARP-1, high-risk neuroblastoma

INTRODUCTION

Neuroblastoma is the most common extra-cranial solid tumor in childhood with only up to 50% 5-year survival rate in high-risk patients (1). Relapsed cases are often managed with iodine-131-metaiodobenzylguanidine (^{131}I -MIBG) radiopharmaceutical therapy, but its sub-optimal therapeutic efficacy with very low complete response rate remains unsatisfactory (2). The main limitation of ^{131}I -MIBG therapy is the low linear energy transfer (LET) of beta particles, which are unable to produce sufficient radiation fields for lethal DNA damage in micrometastatic disease (3).

Our group has recently developed an ^{211}At -labeled radiopharmaceutical, ^{211}At -MM4, which showed strong anti-tumor efficacy in neuroblastoma (4). In contrast to MIBG which targets the norepinephrine transporter, ^{211}At -MM4 binds to poly(ADP-ribose) polymerase 1 (PARP-1), a chromatin-associated protein overexpressed in neuroblastoma (4).

PARP-targeted radiopharmaceutical therapeutics (PARP-RPTs) not only enable efficient delivery of radiation to DNA, but also allow using other types of high-LET therapeutic radiation that otherwise would not penetrate cells. Auger electrons are emitted in cascades and have low energy of up to 100 keV with $<0.5\ \mu\text{m}$ range (5). The most extensively investigated Auger emitter is iodine-125 with 60-day half-life and 20-25 Auger emissions per decay (5), exhibiting high relative biological effectiveness (RBE) and low oxygen enhancement ratio characteristic of high-LET radiation when integrated into DNA (6).

Therefore, targeting PARP-1 with an Auger-emitting ^{125}I -labeled small molecule is an attractive strategy to deliver high-LET radiation to neuroblastoma. One such radiopharmaceutical is ^{125}I -KX1, an analog of ^{211}At -MM4 where ^{211}At is replaced by ^{125}I (4, 7). While ^{125}I -KX1 has been previously described as a biomarker to quantify PARP-1 expression in ovarian cancer models (7), its therapeutic use has not been investigated in any cancer models.

In the present study, we used ^{125}I -KX1 to examine the therapeutic potential of a PARP-1-targeted Auger emitter in pre-clinical models of high-risk neuroblastoma (Fig. 1). After characterizing its PARP-

dependent *in vitro* cytotoxicity, we made dosimetry-based comparison of ^{125}I -KX1 to alpha, beta, gamma, and cytoplasmic Auger radiation to evaluate its effectiveness relative to other conventional and experimental therapies. Finally, comparison with its alpha-emitting analog ^{211}At -MM4 was made with *in vivo* tumor dosimetry to explore the feasibility of using Auger-emitting PARP-RPTs for *in vivo* therapy.

MATERIALS AND METHODS

The overall experimental design of the present study has been illustrated on Figure 1.

Chemistry and Radiochemistry

Non-radioactive KX1, ^{125}I -KX1, ^{211}At -MM4, and ^{125}I -MIBG were synthesized as previously described with greater than 95% chemical and radiochemical purity (4,7,8). ^{131}I -KX1 was synthesized in identical manner to ^{125}I -KX1. The specific activities of ^{125}I -KX1/ ^{125}I -MIBG, ^{131}I -KX1, and ^{211}At -MM4 were 81.4 GBq/mmol, 592 GBq/mmol, and 16,021 GBq/mmol respectively.

Cell Culture

Nineteen human neuroblastoma cell lines were obtained from the Children's Hospital of Philadelphia Cell Bank (Supplemental Table 1) and were cultured as previously described (4).

Immunofluorescence Microscopy

In order to characterize the specificity ^{125}I -KX1 Auger-induced DNA damage, IMR-05 and NLF cells were treated with 1.85 MBq/mL ^{125}I -KX1 \pm 500 nM veliparib for 1 hour and were subsequently analyzed by assessing γH2AX (05-636, Millipore, Burlington MA) and PARP-1 (46D11, Cell Signaling Technology, Danvers MA) fluorescence under manufacturer-recommended conditions. Secondary antibodies were used at a 1:200 dilution (Invitrogen #A32723, Invitrogen #A32794). The slides were mounted using Prolong

Glass with NucBlue stain (Invitrogen #P36985) and images were acquired at 40X magnification on a Leica STED 3X Super-resolution Confocal Microscope. Quantification of γ H2AX fluorescence was performed in mapped nuclei by intensity and normalized to nuclei area using the Speckle Counting pipeline of the Cell Profiler software (9). Three random fields of view were quantified per treatment condition.

***In Vitro* Cytotoxicity**

The cytotoxicity of ^{125}I -KX1 was screened in nineteen human neuroblastoma cell lines as previously described (4), with 72-hour treatments of 0.925 Bq/mL - 925 kBq/mL ^{125}I -KX1 compared to 100 pM - 100 μM of KX1 as non-radioactive controls. EC_{50} values of ^{125}I -KX1 were correlated with EC_{50} values of KX1 and published EC_{50} values of ^{211}At -MM4 (4), as well as with PARP-1 mRNA expression levels measured by reverse transcription polymerase chain reaction.

For all downstream experiments, IMR-05 and NLF were chosen as examples of a sensitive and resistant cell line, respectively (Fig. 1). External gamma radiation was delivered with a cesium-137 source at the dose rate of 1.5 cGy/sec, up to 2 Gy total dose for IMR-05 and 6 Gy for NLF. The cells were seeded immediately following the irradiation and survival fraction was quantified after 72 hours as in the ^{125}I -KX1 cytotoxicity assay. The survival fraction was plotted against radiation dose using the linear-quadratic model (10).

As a model for targeted low-LET beta therapy, cytotoxicity assay with ^{131}I -KX1 was performed on IMR-05 and NLF cell lines with dose range of 2.4 kBq/mL - 37 MBq/mL. Cytotoxicity data for ^{211}At -MM4 and unconjugated free ^{211}At (^{211}At -NaAt^x) was obtained from published data as examples of targeted and non-targeted alpha particle therapy, respectively (4). Finally, cytotoxicity assay with ^{125}I -MIBG was performed at the dose range of 0.925 Bq/mL - 925 kBq/mL to model cytoplasmic Auger emitter therapy. ^{125}I -MIBG served as a strict negative radioactive control in lieu of free ^{125}I , which is not taken up by

neuroblastoma cells and therefore only deposits extracellular Auger dose (11). Experiments were completed in triplicates three independent times.

Radiopharmacology

Radioligand saturation binding assay was performed with ^{125}I -KX1 in IMR-05 and NLF cell lines as previously published (4). The maximum number of binding sites (B_{max}) was expressed in targets/cell by normalizing to the cell number using Countess II Automated Cell Counter (Thermo Fisher Scientific, Grand Island, NY). The binding affinity (K_d) of ^{211}At -MM4 was obtained indirectly by comparison to ^{125}I -KX1 binding under non-saturating concentrations up to 37 kBq/mL (Supplemental Equation 1). ^{125}I -MIBG uptake was measured after 2-hour incubation at the non-saturating concentrations used in the cytotoxicity assay (up to 925 kBq/mL) \pm blocking with 10 μM of desipramine (12).

Subcellular Radiation Dosimetry

In order to calculate the radiation dose to the cell nucleus from ^{125}I -KX1, ^{131}I -KX1, ^{125}I -MIBG, and ^{211}At -MM4, on-target cumulated activity (\tilde{A}) was derived from the radiopharmacology data (Supplemental Equation 2). Then, the radiation dose to the cell nucleus was obtained using Monte Carlo simulation with Medical Internal Radiation Dosimetry Cell (MIRDcell) V2.1 as described previously (13). The radii of the cell and its nucleus were measured with phase contrast and fluorescence microscopy with DAPI, respectively.

In order to calculate the cross-dose from neighboring cells, the growth rates of IMR-05 and NLF cell lines were measured by counting the cells daily with Countess II Automated Cell Counter (Thermo Fisher Scientific, Grand Island, NY). Then, the cell numbers, cumulated activity, radionuclide information, and dimensions of the wells in the cytotoxicity assay were applied to the two-dimensional dosimetry model

on MIRDcell to obtain cross-dose values. For nonspecific alpha therapy with $^{211}\text{At-NaAt}^x$, the radiation dose to the culture media at the bottom of the wells was used to represent cellular radiation dose.

With the dosimetric calculations, the cytotoxic dose response curves for the radiopharmaceuticals were transformed to radiation dose response curves based on the linear-quadratic model. Using 50% survival as the reference endpoint, the RBE among the different types of radiation was calculated.

***In Vivo* Tumor Dosimetry with 3-Dimensional Modeling**

In order to compare the therapeutic efficacy of $^{125}\text{I-KX1}$ and $^{211}\text{At-MM4}$ for *in vivo* therapy, radiation dosimetry was performed with densely packed 3-dimensional face-centered cubic modeling of a solid xenograft tumor consisting of spherical IMR-05 tumor cells. Radiation dosimetry was then performed both macroscopically and microscopically. First, per decay event in every tumor cell, radiation dose to the macroscopic tumor volume due to entire particulate energy absorption was calculated. In addition, the subcellular radiation dose to the tumor cell nuclei was calculated by accounting for the self and cross dose contributions based on the geometric distances among tumor cells in the 3-dimensional model. The S-value for cross-dose calculation was obtained for each cell-cell pair on MIRDcell V2.1 (13).

Finally, the nuclear radiation dose per decay event was adjusted by differences in RBE and binding affinity to PARP-1, as well as effective half-lives for $^{125}\text{I-KX1}$ and $^{211}\text{At-MM4}$ from previously published *in vivo* biodistribution data (4,7). The adjusted dosimetry results enabled comparison of equivalent therapeutic administered dose between $^{125}\text{I-KX1}$ and $^{211}\text{At-MM4}$.

Statistical Analysis

The $\log(\text{EC}_{50})$ values between $^{125}\text{I-KX1}$ and KX1 for each cell line were compared using unpaired t-test. Linear regression was performed to determine the variation in $\log(\text{EC}_{50})$ of $^{125}\text{I-KX1}$ with respect to

log(EC₅₀) of KX1 and ²¹¹At-MM4, as well as with respect to PARP-1 mRNA level. γ H2AX fluorescence intensity of the cells treated with ¹²⁵I-KX1 was compared with those of other treatment conditions with unpaired t-test. The B_{max}, K_d, growth rate, log(EC₅₀), and D₅₀ were compared between IMR-05 and NLF cell lines using unpaired t-test. All statistical comparisons were two-tailed and p<0.05 was considered statistically significant. GraphPad Prism 7 (GraphPad Software, San Diego CA) was used to perform all statistical tests and data fitting. Numerical values are reported as mean \pm standard error of measurement (SEM).

RESULTS

Immunofluorescence Microscopy

In IMR-05 and NLF cells, treatment with ¹²⁵I-KX1 caused double strand DNA breaks as visualized with γ H2AX on immunofluorescence microscopy (Fig. 2). γ H2AX was substantially reduced when ¹²⁵I-KX1 binding to PARP-1 was blocked by 500 nM of veliparib.

In Vitro Cytotoxicity of ¹²⁵I-KX1

Compared to the non-radioactive analog KX1, ¹²⁵I-KX1 demonstrated 10⁴ - 10⁶ times greater cytotoxicity than KX1 on a molar scale. (Fig. 3A) (p<0.0001) (Fig. 3B). Sensitivity to ¹²⁵I-KX1 and KX1 was moderately correlated ($R^2=0.58$, p<0.001 for non-zero slope), with exponential increase in sensitivity to ¹²⁵I-KX1 (slope = 2.15 \pm 0.47 on log-log plot) (Fig. 3C). Sensitivity to ¹²⁵I-KX1 and ²¹¹At-MM4 showed a strong positive correlation ($R^2=0.93$, p<0.0001 for non-zero slope) with one-to-one relationship (slope = 1.07 \pm 0.08) (Fig. 3D). PARP-1 mRNA level was only minimally correlated with sensitivity to ¹²⁵I-KX1 ($R^2=0.23$, p<0.05 for non-zero slope) (Fig. 3E).

While IMR-05 cells were more sensitive to all forms of radionuclide therapy than NLF (p<0.0001), different radiopharmaceuticals maintained the same order of potency relative to one another in both cell

lines (Fig. 4A). The most potent radiopharmaceutical was $^{211}\text{At-MM4}$, followed by $^{125}\text{I-KX1}$, $^{211}\text{At-NaAt}^x$, $^{131}\text{I-KX1}$, and $^{125}\text{I-MIBG}$ (Supplemental Table 2). As with radiopharmaceuticals, external gamma irradiation was more lethal with lower D_{50} in IMR-05 (0.71 ± 0.02 Gy) compared to NLF (3.7 ± 0.1 Gy) ($p < 0.0001$) (Fig. 4B).

Radiopharmacology

Radioligand binding assays revealed that IMR-05 had higher $^{125}\text{I-KX1}$ uptake ($p < 0.0001$) but lower $^{125}\text{I-MIBG}$ uptake ($p < 0.0001$) than NLF whereas the binding affinity of $^{125}\text{I-KX1}$ ($p = 0.40$) and $^{211}\text{At-MM4}$ ($p = 0.38$) between the two cell lines was similar (Supplemental Fig. 1A-C), suggesting different expression levels of structurally identical target proteins. IMR-05 demonstrated higher growth rate than NLF ($p < 0.0001$) (Supplemental Fig. 1D), leading to higher cross-dose deposition due to proximity between adjacent cells. On microscopy, the nuclear and cellular radii of IMR-05 cells were measured to the nearest whole number at $6 \mu\text{m}$ and $8 \mu\text{m}$, respectively, compared to NLF with $9 \mu\text{m}$ and $12 \mu\text{m}$ radii (Supplemental Fig. 1E).

Subcellular Radiation Dosimetry

Despite the wide variation in EC_{50} , dosimetric analysis revealed that the RBE of the radiopharmaceuticals are within the same order of magnitude. Without PARP-1 targeting, alpha particles from $^{211}\text{At-NaAt}^x$ demonstrated 3.6-3.7 times greater RBE compared to gamma irradiation (Fig. 4B). On the other hand, cytoplasmic Auger radiation from $^{125}\text{I-MIBG}$ was slightly weaker than gamma radiation in IMR-05 (RBE=0.65) and equally efficacious in NLF (RBE=1.0).

Among the PARP-1-targeted radiopharmaceuticals, alpha-emitting $^{211}\text{At-MM4}$ remained the most effective with RBE of 6.3-6.7 compared to high-energy beta-emitting $^{131}\text{I-KX1}$ (Fig. 4C). In contrast to $^{125}\text{I-MIBG}$, Auger-emitting $^{125}\text{I-KX1}$ was more effective than $^{131}\text{I-KX1}$ with RBE of 1.8-1.9. As expected from their high LET and/or low dose rate, all the targeted radiopharmaceuticals demonstrated linear (α -dominant)

survival curves in the linear-quadratic model (Supplemental Table 3) (10). Therefore, the RBE values were maintained across different choice of endpoints. A summary of *in vitro* dosimetry results and RBE has been provided on Table 1.

***In Vivo* Tumor Dosimetry with 3-Dimensional Modeling**

The face-centered cubic tumor model and target volumes are represented in Figures 5A and 5B, respectively. When the radiation dose to the entire tumor volume was considered, $^{211}\text{At-MM4}$ deposited 350 times more dose to the tumor per decay event compared to $^{125}\text{I-KX1}$, owing to the much higher energy carried by the alpha particles than Auger electrons. Compared to the entire tumor dose, radiation dose only to the tumor cell nuclei was higher with $^{125}\text{I-KX1}$ due to its highly localized dose deposition centered in the nuclei, whereas it was unchanged with $^{211}\text{At-MM4}$ (Fig. 5C). Therefore, $^{211}\text{At-MM4}$ deposited only 150 times higher tumor nuclei dose per decay event compared to $^{125}\text{I-KX1}$.

Previously published *in vivo* biodistribution results of $^{211}\text{At-MM4}$ and $^{125}\text{I-KX1}$ have been remarkably similar, owing to their identical chemical structures except for the radionuclide (4, 7). Although the effective half-life of $^{125}\text{I-KX1}$ (1.5 hours) is approximately 36% longer than that of $^{211}\text{At-MM4}$ (1.1 hours) due to the longer physical half-life of ^{125}I , it has approximately 35% less target binding affinity ($K_d=5.8$ nM) than $^{211}\text{At-MM4}$ ($K_d=4.3$ nM) in IMR-05 cell line. Given the small differences in biological distribution of the two compounds, the primary difference between $^{211}\text{At-MM4}$ and $^{125}\text{I-KX1}$ for *in vivo* efficacy estimation lies in the RBE of 3.5. Taking into account the 3.5-fold higher RBE and the 150-fold greater nuclear radiation dose per decay, both in favor of $^{211}\text{At-MM4}$, administration of 530-fold greater activity of $^{125}\text{I-KX1}$ is required for equivalent *in vivo* efficacy as $^{211}\text{At-MM4}$.

DISCUSSION

The present study evaluated the feasibility of chromatin-targeted high-LET Auger electron therapy in high-risk neuroblastoma with the iodinated PARP-1 inhibitor $^{125}\text{I-KX1}$. We first validated the basic mechanism of $^{125}\text{I-KX1}$ -induced cytotoxicity: $^{125}\text{I-KX1}$ causes double strand DNA breaks dependent on binding to active PARP-1 (Fig. 2) and not associated with pharmacologic inhibition (Fig. 3A-B).

Since sensitivity to PARPi such as KX1 is strongly correlated with the number of pharmacologically active binding sites (B_{max}) (7), the correlation between sensitivity to $^{125}\text{I-KX1}$ and KX1 (Fig. 3C) reflects the relationship between $^{125}\text{I-KX1}$ -induced cytotoxicity and its degree of target binding. The weak correlation presented between sensitivity to $^{125}\text{I-KX1}$ and PARP-1 mRNA should be interpreted with caution as previous reports demonstrated a lack of correlation between PARP-1 mRNA expression and protein level (14). Although, an association is evident between $^{125}\text{I-KX1}$ sensitivity and PARP-1 mRNA expression future studies will be needed to identify the most appropriate method for quantifying PARP-1.

The RBE values of ^{125}I obtained from subcellular dosimetry in IMR-05 and NLF cell lines were in accordance with the previous understanding of Auger therapy. RBE of cytoplasmic $^{125}\text{I-MIBG}$ was at best equal to gamma irradiation, and was slightly lower at 0.65 in IMR-05 cells due to the loss of quadratic (β) cell kill at low dose rate (Supplemental Table 3) (10). The RBE of $^{125}\text{I-KX1}$ at approximately 2 demonstrates the high radiotoxicity of Auger therapy, but it is slightly lower than previously documented RBE of 4-5 for DNA-incorporated $^{125}\text{IdUrd}$ vs. $^{131}\text{IdUrd}$ (15). The lower RBE likely results from the distance of 50 Å from the PARP-1 active site to DNA (Supplemental Fig. 2) (16-18), which further increases when PARP-1 is indirectly bound to DNA via chromatin-associated proteins. Even angstrom-level increase in distance from DNA leads to precipitous decrease in biological effectiveness of ^{125}I , where 12 Å is the critical distance (19). Rather, the observed RBE of $^{125}\text{I-KX1}$ up to 4 against gamma irradiation matches those of nuclear-targeted Auger emitters noncovalently bound to DNA (20). Therefore, $^{125}\text{I-KX1}$

demonstrated high RBE corresponding to its subcellular targeting, which serves as a key component of its toxicity.

Compared to previously described therapeutic Auger emitters, the major significance of ^{125}I -KX1 is the combination of high RBE and target specificity. Attempts to specifically deliver Auger emitters with antibodies and small molecules such as ^{125}I -MIBG suffered from low cytotoxicity due to non-nuclear localization (21,22). DNA-targeting Auger emitters including ^{125}I dUrd have demonstrated high effectiveness, but the ubiquitous nature of DNA leads to poor target specificity and high normal tissue toxicity (23). While endocrine receptors have been targeted with Auger emitters (24,25), the receptors are not always bound to DNA and a specific endocrine receptor target has not been found in neuroblastoma. A previous study used indium-111-labeled oligonucleotides complementary to *N-myc* in order to specifically deliver Auger radiation to neuroblastoma (26). While reduced expression of *N-myc* led to slowed growth rate, the tumor cells remained viable due to the very limited nuclear uptake of oligonucleotides in unaltered form (26,27).

Interestingly, the increase in RBE with PARP-1-targeting was observed not only with ^{125}I but also with ^{211}At , which can be explained by two properties specific to ^{211}At . First, alpha emission from ^{211}At is accompanied by recoil of the parent nucleus to the opposite direction that delivers high-LET radiation with a range of 90 nm, and therefore contributes to cytotoxicity only when the decay occurs in the nucleus (28). Second, ^{211}At also has lesser-known emission of approximately 6.3 Auger electrons per decay, which deposit more radiation dose than alpha particles within 10 nm (29). Despite the higher Auger yield of ^{125}I , the combined effect of recoil and Auger emission from ^{211}At decay makes PARP-1-targeted ^{211}At therapy a more effective approach.

The benefit of ^{211}At -MM4 therapy over ^{125}I -KX1 was also demonstrated by *in vivo* tumor dosimetry. Despite ^{125}I -KX1's focused delivery of radiation to the cell nuclei, ^{211}At -MM4's much higher nuclear dose per decay and favorable RBE led to two-orders-of-magnitude higher therapeutic potency per decay. In the

setting of irreversible DNA integration where the number of ^{125}I dUrd decays was 10-fold higher than that of ^{211}At dUrd, approximately 30 times more tumor dose was deposited by ^{211}At dUrd, congruent with the results of our organ level dosimetry. The previously established lowest effective therapeutic dose of ^{211}At -MM4 in IMR-05 tumor-bearing mice was 555 kBq (4), which would translate to 296 MBq of ^{125}I -KX1. We predicted this dose would not be safe in mice based on toxicity of two different Auger emitting therapeutics investigated in previous studies; an ^{125}I -labeled monoclonal antibody had the median toxic dose of 111 MBq in mice, and more cytotoxic DNA-incorporating ^{125}I dUrd had the median toxic dose of 74 MBq in rats (15,30). In addition, ^{131}I -MIBG shows anti-tumor activity in neuroblastoma models at 9.4 MBq which questions the utility of Auger therapy in macroscopic disease (unpublished data). Another limitation of ^{125}I -KX1 is its remarkably long physical half-life of 60 days compared to the biological half-life of 1.5 hours, as well as its significant target-specific uptake in the spleen and pancreas (7).

Although Auger therapy may be impractical for therapeutic evaluation in solid tumor models, the present study suggests its potential value in micrometastatic disease. We demonstrated that a PARP-1-targeted Auger emitter has enhanced RBE over beta-emitting analogues at the cellular level. The therapeutic ratio of Auger emitters would be maximized in micrometastatic setting by providing single-cell lethality without compromising surrounding healthy tissue. Other aspects to improve translatability of PARP-RPTs for Auger therapy include increasing on-target drug retention at PARP-1 through medicinal chemistry approaches or using shorter-lived auger emitters such as bromine-77 to overcome the challenges of using long-lived isotopes.

CONCLUSION

In this work we showed Auger emitters are cytotoxic to high-risk neuroblastoma with high-LET properties when targeted to PARP-1. However, the utility of systemically administered Auger therapy with unfavorable in vivo kinetics remains questionable for evaluation in solid tumor models.

KEY POINTS

QUESTION: Do Auger emitters exhibit high-LET properties when targeted to PARP-1 and can they be used to treat radiosensitive cancers?

PERTINENT FINDINGS: PARP-1-targeted Auger emitters exhibit high-LET properties with enhanced relative biological effectiveness (RBE) in neuroblastoma over gamma and beta radiation, but with lower RBE compared to alpha radiation. Dosimetric comparisons between PARP-1-targeted alpha and Auger radiation revealed that alpha radiation deposits much higher dose to the tumor than Auger radiation, primarily attributed to the low energy of Auger electrons.

IMPLICATIONS FOR PATIENT CARE: PARP-1 has emerged as a clinical drug target for treating cancers with DNA repair deficiencies, and our studies show that targeting PARP-1 with alpha and Auger radiation is potentially cytotoxic in neuroblastoma warranting future clinical translation.

REFERENCES

1. Matthay KK, Maris JM, Schleiermacher G, et al. Neuroblastoma. *Nat Rev Dis Primers*. 2016;2:16078.
2. Pandit-Taskar N, Modak S. Norepinephrine transporter as a target for imaging and therapy. *J Nucl Med*. 2017;58:39s-53s.
3. Carlin S, Akabani G, Zalutsky MR. In vitro cytotoxicity of (211)at-astatide and (131)I-iodide to glioma tumor cells expressing the sodium/iodide symporter. *J Nucl Med*. 2003;44:1827-1838.
4. Makvandi M, Lee H, Puentes LN, et al. Targeting PARP-1 with alpha-particles is potentially cytotoxic to human neuroblastoma in pre-clinical models. *Mol Cancer Ther*. 2019.
5. Falk SJ, Lee J, Sekulic N, Sennett MA, Lee TH, Black BE. CENP-C directs a structural transition of CENP-A nucleosomes mainly through sliding of DNA gyres. *Nat Struct Mol Biol*. 2016;23:204-208.
6. Koch CJ, Burki HJ. The oxygen-enhancement ratio for reproductive death induced by 3H or 125I damage in mammalian cells. *Int J Radiat Biol Relat Stud Phys Chem Med*. 1975;28:417-425.
7. Makvandi M, Xu K, Lieberman BP, et al. A radiotracer strategy to Quantify PARP-1 expression in vivo provides a biomarker that can enable patient selection for PARP inhibitor therapy. *Cancer Res*. 2016;76:4516-4524.
8. Batra V, Makvandi M, Zuppa AF, et al. Dexmedetomidine does not interfere with meta-iodobenzylguanidine (MIBG) uptake at clinically relevant concentrations. *Pediatr Blood Cancer*. 2017;64.
9. Kametsky L, Jones TR, Fraser A, et al. Improved structure, function and compatibility for CellProfiler: modular high-throughput image analysis software. *Bioinformatics*. 2011;27:1179-1180.
10. Kassis AI. Therapeutic radionuclides: biophysical and radiobiologic principles. *Semin Nucl Med*. 2008;38:358-366.
11. Klutz K, Russ V, Willhauck MJ, et al. Targeted radioiodine therapy of neuroblastoma tumors following systemic nonviral delivery of the sodium iodide symporter gene. *Clin Cancer Res*. 2009;15:6079-6086.

12. Werner RA, Kobayashi R, Javadi MS, et al. Impact of novel antidepressants on cardiac (123)I-metaiodobenzylguanidine uptake: experimental studies on SK-N-SH cells and healthy rabbits. *J Nucl Med.* 2018;59:1099-1103.
13. Vaziri B, Wu H, Dhawan AP, Du P, Howell RW, Committee SM. MIRD pamphlet No. 25: MIRDcell V2.0 software tool for dosimetric analysis of biologic response of multicellular populations. *J Nucl Med.* 2014;55:1557-1564.
14. Bieche I, Pennaneach V, Driouch K, et al. Variations in the mRNA expression of poly(ADP-ribose) polymerases, poly(ADP-ribose) glycohydrolase and ADP-ribosylhydrolase 3 in breast tumors and impact on clinical outcome. *Int J Cancer.* 2013;133:2791-2800.
15. Kassis AI, Kirichian AM, Wang K, Semnani ES, Adelstein SJ. Therapeutic potential of 5-[125I]iodo-2'-deoxyuridine and methotrexate in the treatment of advanced neoplastic meningitis. *Int J Radiat Biol.* 2004;80:941-946.
16. Langelier MF, Planck JL, Roy S, Pascal JM. Structural basis for DNA damage-dependent poly(ADP-ribose)ylation by human PARP-1. *Science.* 2012;336:728-732.
17. Rose AS, Bradley AR, Valasatava Y, Duarte JM, Prlic A, Rose PW. NGL viewer: web-based molecular graphics for large complexes. *Bioinformatics.* 2018;34:3755-3758.
18. Berman HM, Westbrook J, Feng Z, et al. The Protein Data Bank. *Nucleic Acids Res.* 2000;28:235-242.
19. Balagurumoorthy P, Xu X, Wang K, Adelstein SJ, Kassis AI. Effect of distance between decaying (125)I and DNA on Auger-electron induced double-strand break yield. *International journal of radiation biology.* 2012;88:998-1008.
20. Humm JL, Howell RW, Rao DV. Dosimetry of Auger-electron-emitting radionuclides: report no. 3 of AAPM Nuclear Medicine Task Group No. 6. *Med Phys.* 1994;21:1901-1915.
21. Rutgers M, Buitenhuis CK, van der Valk MA, Hoefnagel CA, Voute PA, Smets LA. [(131)I] and [(125)I] metaiodobenzylguanidine therapy in macroscopic and microscopic tumors: a comparative study in SK-N-SH human neuroblastoma and PC12 rat pheochromocytoma xenografts. *Int J Cancer.* 2000;90:312-325.
22. Govindan SV, Goldenberg DM, Elsamra SE, et al. Radionuclides linked to a CD74 antibody as therapeutic agents for B-cell lymphoma: comparison of Auger electron emitters with beta-particle emitters. *J Nucl Med.* 2000;41:2089-2097.

23. Kassis AI. The amazing world of auger electrons. *Int J Radiat Biol.* 2004;80:789-803.
24. Yasui LS, Hughes A, Desombre ER. Cytotoxicity of ¹²⁵I-oestrogen decay in non-oestrogen receptor-expressing human breast cancer cells, MDA-231 and oestrogen receptor-expressing MCF-7 cells. *International Journal of Radiation Biology.* 2001;77:955-962.
25. Kiess AP, Minn I, Chen Y, et al. Auger radiopharmaceutical therapy targeting prostate-specific membrane antigen. *J Nucl Med.* 2015;56:1401-1407.
26. Watanabe N, Sawai H, Ogihara-Umeda I, et al. Molecular therapy of human neuroblastoma cells using Auger electrons of ¹¹¹In-labeled N-myc antisense oligonucleotides. *J Nucl Med.* 2006;47:1670-1677.
27. Buchegger F, Perillo-Adamer F, Dupertuis YM, Bischof Delaloye A. Auger radiation targeted into DNA: a therapy perspective. *European Journal of Nuclear Medicine and Molecular Imaging.* 2006;33:1352-1363.
28. Zalutsky MR, Vaidyanathan G. Astatine-211-labeled radiotherapeutics: an emerging approach to targeted alpha-particle radiotherapy. *Curr Pharm Des.* 2000;6:1433-1455.
29. Unak T. Some microdosimetric data on Astatine-211. *Appl Radiat Isot.* 2003;58:115-117.
30. Behr TM, Sgouros G, Vougiokas V, et al. Therapeutic efficacy and dose-limiting toxicity of Auger-electron vs. beta emitters in radioimmunotherapy with internalizing antibodies: evaluation of ¹²⁵I- vs. ¹³¹I-labeled CO17-1A in a human colorectal cancer model. *Int J Cancer.* 1998;76:738-748.

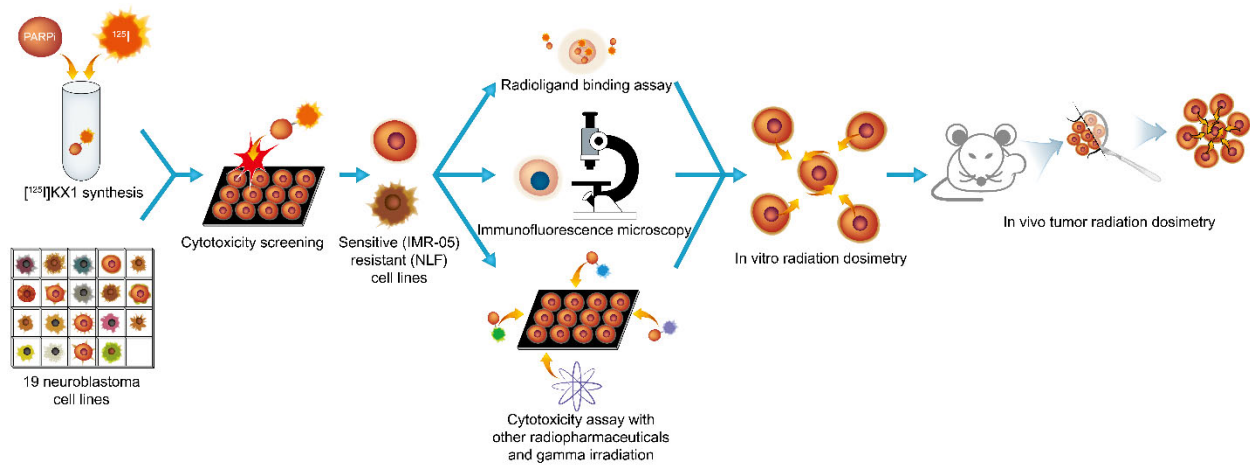


FIGURE 1. Workflow for pre-clinical evaluation of ^{125}I -KX1 in high-risk neuroblastoma. Nineteen human neuroblastoma cell lines were screened for cytotoxic sensitivity to ^{125}I -KX1. IMR-05 and NLF were chosen as representative cell lines for downstream experiments. Radioligand binding assay, immunofluorescence microscopy, and further cytotoxicity screening were followed by *in vitro* and *in vivo* radiation dosimetry.

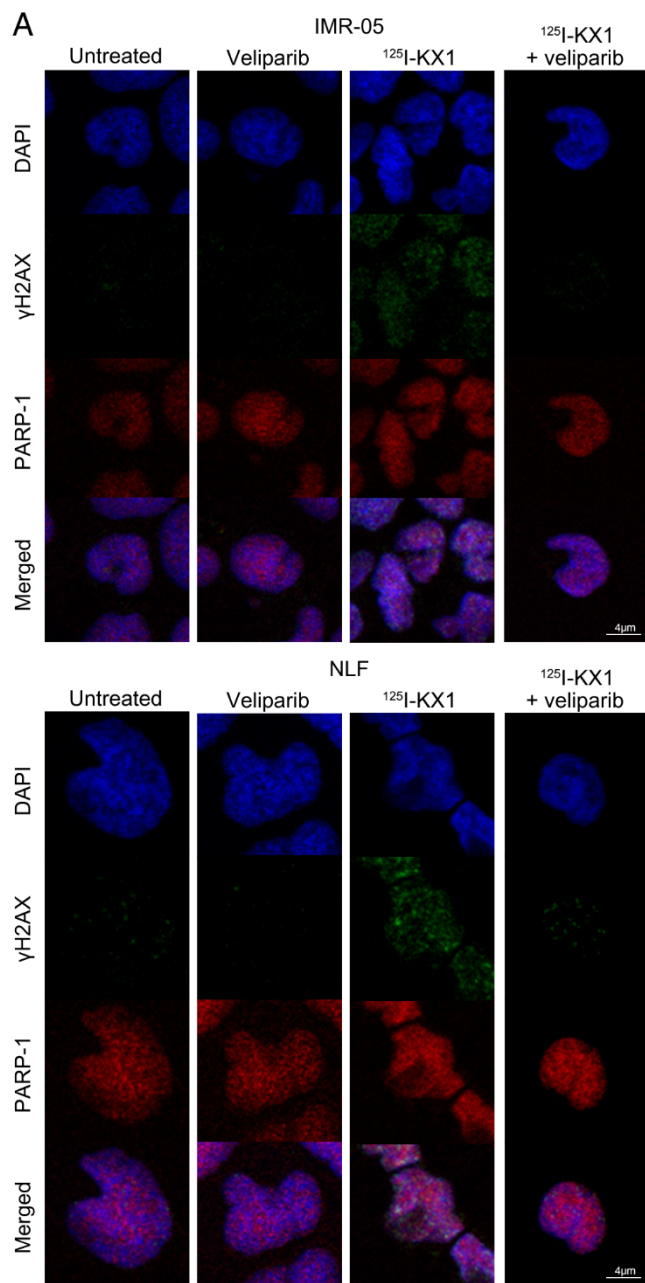
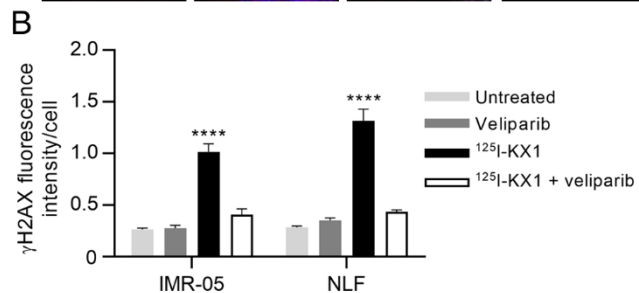


FIGURE 2. Dependency of ¹²⁵I-KX1-induced DNA damage on PARP-1. **(A)** Immunofluorescence microscopy images with γH2AX show ¹²⁵I-KX1-induced double strand DNA breaks, which were substantially blocked with veliparib. **(B)** Quantification of the fluorescence intensity revealed statistically significant γH2AX signal increase with ¹²⁵I-KX1 relative to the other conditions. ****p<0.0001.



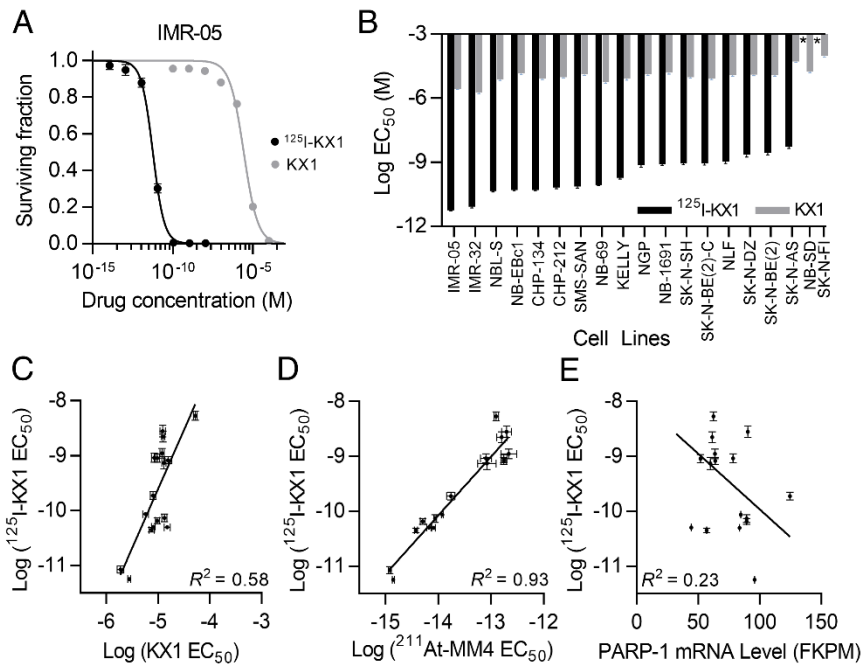


FIGURE 3. *In vitro* studies evaluating ^{125}I -KX1-induced cytotoxicity in neuroblastoma cell lines. **(A)** Representative cytotoxic dose response curves for ^{125}I -KX1 and non-radioactive KX1 in a neuroblastoma cell line (IMR-05). **(B)** Waterfall plot of EC_{50} values for ^{125}I -KX1 and KX1 in a panel of 19 neuroblastoma cell lines. * represents <50% cell kill in the dose range tested. ($p < 0.0001$ for ^{125}I -KX1 vs. KX1 in all 17 cell lines with >50% cytotoxicity). Sensitivity to ^{125}I -KX1 was correlated with sensitivity to **(C)** KX1 and **(D)** ^{211}At -MM4, but minimally with **(E)** PARP-1 mRNA level.

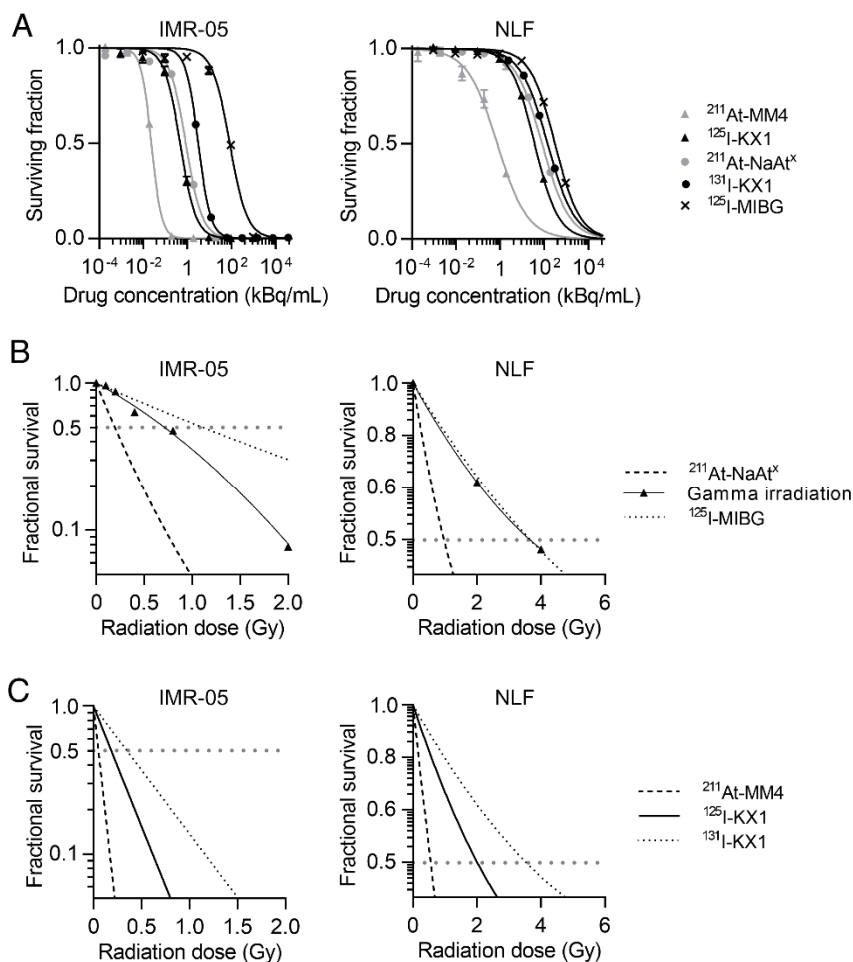


FIGURE 4. Response to various types of radiotherapy with radiation dosimetry. **(A)** Cytotoxic dose response curves for $^{211}\text{At-MM4}$, $^{125}\text{I-KX1}$, $^{211}\text{At-NaAt}^x$, $^{131}\text{I-KX1}$, and $^{125}\text{I-MIBG}$ based on radioactivity concentration. **(B)** Cell survival curves for non-targeted radiotherapy with external gamma irradiation, $^{211}\text{At-NaAt}^x$, and $^{125}\text{I-MIBG}$ based on radiation dose to the cell nuclei. **(C)** Cell survival curves for PARP-RPTs ($^{125}\text{I-KX1}$, $^{131}\text{I-KX1}$, and $^{211}\text{At-MM4}$) based on radiation dose to the cell nuclei.

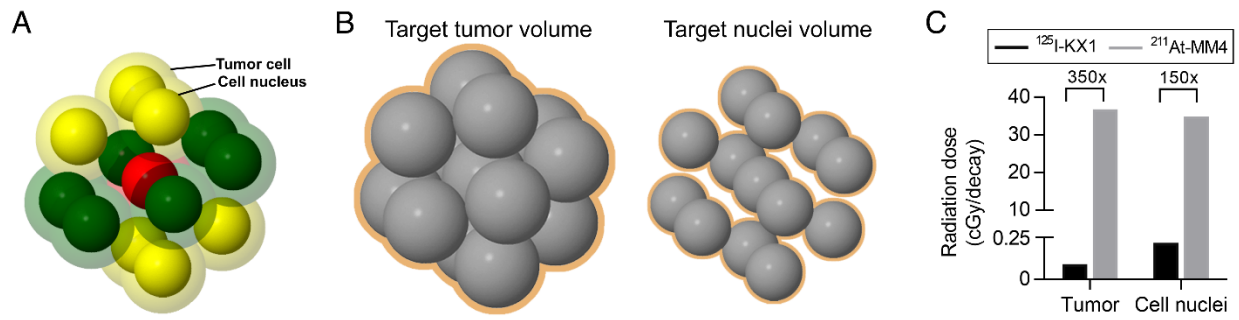


FIGURE 5. *In vivo* tumor radiation dosimetry with 3D modeling. **(A)** Diagram showing a tumor cell and its nearest neighbors. The cell (red) receives self-dose as well as cross-dose from the neighboring cells on the same (green) and different (yellow) planes. **(B)** Target volume diagrams for conventional organ-level dosimetry (whole tumor) and micro-dosimetry (cell nuclei). **(C)** Dose-per-decay-event comparison of $^{211}\text{At-MM4}$ and $^{125}\text{I-KX1}$.

TABLE 1. Summary of *in vitro* dosimetry

	IMR-05	NLF
D₅₀ (Gy)		
¹²⁵ I-KX1	0.18 ± 0.01	2.0 ± 0.1
¹³¹ I-KX1	0.35 ± 0.01	3.5 ± 0.3
¹²⁵ I-MIBG	1.1 ± 0.1	3.7 ± 0.3
²¹¹ At-MM4	0.051 ± 0.002	0.56 ± 0.07
²¹¹ At-NaAt ^x	0.20 ± 0.01	1.0 ± 0.1
External gamma	0.71 ± 0.02	3.7 ± 0.1
RBE for non-targeted therapy		
¹²⁵ I-MIBG vs. gamma	0.65	1.0
²¹¹ At-NaAt ^x vs. gamma	3.6	3.7
²¹¹ At-NaAt ^x vs. ¹²⁵ I-MIBG	5.5	3.7
RBE for targeted therapy		
¹²⁵ I-KX1 vs. ¹³¹ I-KX1	1.9	1.8
²¹¹ At-MM4 vs. ¹³¹ I-KX1	6.7	6.3
²¹¹ At-MM4 vs. ¹²⁵ I-KX1	3.5	3.6

*Values are reported as mean ± SEM.

SUPPLEMENTAL TABLE 1. Cell lines evaluated in this study and relevant mutations.

Cell line	Mutation
IMR-05	neurofibromatosis type 1
IMR-32	N/A
NBL-S	anaplastic lymphoma kinase
NB-EBc1	tumor protein p53
CHP-134	N/A
CHP-212	anaplastic lymphoma kinase
SMS-SAN	tumor protein p53
NB-69	tumor protein p53
KELLY	N/A
NGP	N/A
NB-1691	N/A
SK-N-SH	N/A
SK-N-BE(2)-C	N/A
NLF	N/A
SK-N-DZ	N/A
SK-N-BE(2)	N/A
SK-N-AS	N/A
NB-SD	N/A
SK-N-FI	N/A

*N/A=not applicable

SUPPLEMENTAL TABLE 2. EC₅₀ values of radionuclide therapy in IMR-05 and NLF

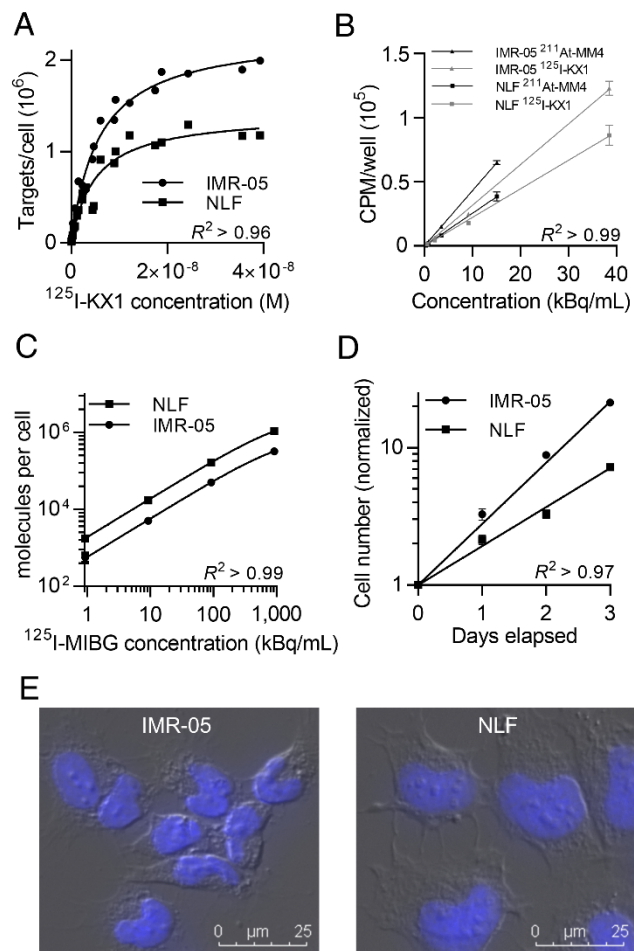
	IMR-05	NLF
[²¹¹ At]MM4	620 ± 30 pCi/mL	20 ± 4 nCi/mL
[¹²⁵ I]KX1	12.5 ± 0.9 nCi/mL	980 ± 60 nCi/mL
[²¹¹ At]NaAt ^x	22.6 ± 1.4 nCi/mL	2.1 ± 0.2 μCi/mL
[¹³¹ I]KX1	82.8 ± 0.8 nCi/mL	3.8 ± 0.1 μCi/mL
[¹²⁵ I]MIBG	2.2 ± 0.2 μCi/mL	8.2 ± 0.5 μCi/mL

*Values are reported as mean ± SEM.

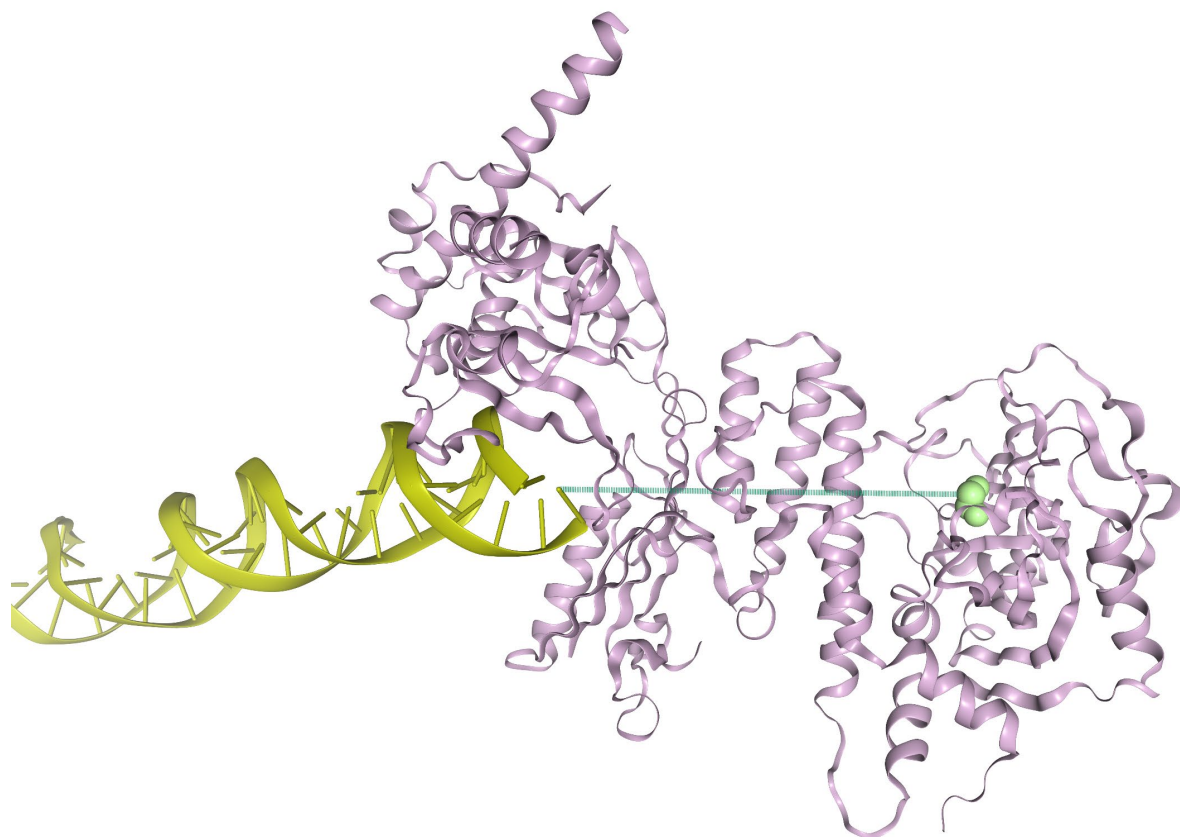
SUPPLEMENTAL TABLE 3: Parameters of IMR-05 and NLF in the linear-quadratic model

	IMR-05		NLF	
	α	β	α	β
[¹²⁵ I]KX1	3.8 ± 0.2	N/A	0.42 ± 0.03	N/A
[¹³¹ I]KX1	2.00 ± 0.03	N/A	0.25 ± 0.01	N/A
[¹²⁵ I]MIBG	0.65 ± 0.09	N/A	0.23 ± 0.02	N/A
[²¹¹ At]MM4	13.6 ± 0.6	N/A	1.3 ± 0.2	N/A
[²¹¹ At]NaAt ^x	3.7 ± 0.2	N/A	0.86 ± 0.08	N/A
External gamma	0.81 ± 0.06	0.22 ± 0.06	0.25 ± 0.01	N/A

*Values are reported as mean ± SEM. N/A=not applicable (approximately zero)



SUPPLEMENTAL FIGURE 1. (A) Radioligand saturation binding study with [^{125}I]KX1 revealed higher B_{max} in IMR-05 ($2.30 \pm 0.07 \times 10^6$ targets/cell) than NLF ($1.41 \pm 0.07 \times 10^6$ targets/cell) but similar K_d (5.8 ± 0.5 nM in IMR-05; 5.1 ± 0.8 nM in NLF). **(B)** Comparison of target binding affinity between [^{125}I]KX1 and [^{211}At]MM4 under non-saturating conditions yielded similar K_d of [^{211}At]MM4 in IMR-05 (4.3 ± 0.5 nM) and NLF (4.5 ± 0.9 nM). **(C)** Direct measurement of cellular [^{125}I]MIBG uptake at cytotoxic concentrations showed 3.29 ± 0.07 times greater uptake in NLF compared to IMR-05. **(D)** IMR-05 and NLF cell lines demonstrated exponential growth pattern with doubling times of 16.2 ± 0.1 hours and 25.5 ± 0.5 hours, respectively. **(E)** Bright field and fluorescence microscopy with DAPI staining allowed measurements of nuclear and cellular radii in IMR-05 ($6 \mu\text{m}$ and $8 \mu\text{m}$) and NLF ($9 \mu\text{m}$ and $12 \mu\text{m}$) cells.



SUPPLEMENTAL FIGURE 2. Three-dimensional structure of PARP1 (purple) bound to DNA (yellow). The distance from the PARP1 active site (green) to DNA was measured at 50.0 Å (dotted line) (16-18).

SUPPLEMENTAL EQUATION 1. Calculation of the binding affinity (K_d) of [^{211}At]MM4 under non-saturating conditions

When $[\text{Ligand}] \ll K_d$ (less than 1%),

$$(\text{Specific binding}) = \frac{B_{\max}[\text{Ligand}]}{K_d + [\text{Ligand}]} \approx \frac{B_{\max}[\text{Ligand}]}{K_d}$$

Then, solving for B_{\max} yields

$$B_{\max} = \frac{(\text{Specific binding})(K_d)}{[\text{Ligand}]} = \alpha \cdot K_d$$

where α is the slope of the specific binding vs. $[\text{Ligand}]$ plot.

Since B_{\max} is shared between [^{125}I]KX1 and [^{211}At]MM4,

$$\alpha_{(MM4)} \cdot K_{d(MM4)} = \alpha_{(KX1)} \cdot K_{d(KX1)}$$

Therefore, solving for $K_{d(MM4)}$ yields

$$K_{d(MM4)} = \frac{\alpha_{(KX1)} \cdot K_{d(KX1)}}{\alpha_{(MM4)}}$$

SUPPLEMENTAL EQUATION 2. Calculation of cumulated activity

Let

B = number of bound molecules per cell at equilibrium

A_s = specific activity (Bq/moles)

N_A = Avogadro's number

$t_{1/2}$ = physical half-life

T = duration of treatment

t = time

Then, the activity of bound molecules in the cell can be represented as a function of time:

$$A(t) = \frac{B}{N_A} \cdot A_s \cdot e^{-\lambda t}$$

where $\lambda = \ln(2)/t_{1/2}$.

Then, the cumulated activity \tilde{A} can be obtained by integrating $A(t)$ over the duration of treatment:

$$\tilde{A} = \int_0^T A(t) dt = \int_0^T \frac{B}{N_A} \cdot A_s \cdot e^{-\lambda t} dt = \frac{B}{N_A} \cdot A_s \cdot \left(\frac{1 - e^{-\lambda T}}{\lambda} \right)$$